Controlling clouds-to-scars dislocations' transitions on spherical crystal shells

Davidyan, S.; Matoz-Fernandez, D.A.; Butenko, A.V.; García-Aguilar, I.; Giomi, L.; Sloutskin, E.

Controlling clouds-to-scars dislocations' transitions on spherical crystal shells

Shirel Davidyan,[1] Daniel A. Matoz-Fernandez,[2] Alexander V. Butenko,[1] Ireth García-Aguilar,[3,*] Luca Giomi,[3,†] and Eli Sloutskin[1,‡]

[1]*Physics Department and Institute of Nanotechnology & Advanced Materials, Bar-Ilan University, Ramat-Gan 5290002, Israel*
[2]*Department of Theoretical Physics, Complutense University of Madrid, Madrid, 28040, Spain*
[3]*Instituut-Lorentz, Universiteit Leiden, P.O. Box 9506, 2300 RA Leiden, The Netherlands*

(Received 21 May 2024; revised 1 August 2024; accepted 9 October 2024; published 4 November 2024)

The closed topology of spherical crystals renders the presence of topological defects inevitable. These defects can organize in a plethora of different structures, such as "clouds" or grain boundary "scars", challenging for theoretical modeling and experimental visualization. Visualizing the defects by fluorescent dye adsorption, we reveal ion concentration control of a clouds-to-scars transition, which we attribute to commonly neglected defects' core energy. The consequent line tension energy probes the defects' molecular scale energetics, enabling pattern tuning for future applications.

DOI: 10.1103/PhysRevResearch.6.043098

I. INTRODUCTION

Oil-in-water [1] and water-in-oil [2] droplets of many common surfactant-stabilized emulsions exhibit an interfacial freezing transition [3], where a mixed oil:surfactant hexagonally packed crystalline monolayer self-assembles at the droplet's interface [4,5]. This transition takes place at a chemical composition-dependent temperature $T = T_s$, with the droplets' liquid bulk phases coexisting with the interfacial crystalline monolayer down to the bulk freezing temperature T_f. In this temperature range [2,6], these emulsion droplets exhibit spectacular examples of self-organization: spontaneous division [3,7], self-propulsion [1,8], shape transformations, such as faceting [5,9] and the formation of tentaclelike protrusions [1], and other unusual effects [10–12], rendering them a unique model system for biomimicry [5,13,14] and smart material applications [5,7]. While the origin of these phenomena is, to a large extent, still debated [5,15], it has recently become evident how *geometrical frustration*, resulting from the incompatibility between the hexagonal crystalline order and the closed topology of the droplets' surfaces, plays a central role in many of the observed phenomena [1,13,15–17]. This frustration is described in terms of the topological charge $q_\alpha = 6 - c_\alpha$, where c_α denotes the number of neighbors, indicating the deviation of the αth lattice site from the planar energy-minimizing sixfold coordination. Consequently, 5-fold and 7-fold *disclinations* are analogous to $+1$ and -1 elementary charges, respectively, while $5-7$ pairs, known as *dislocations*, resemble neutral electric dipoles. While generally defect-free on the plane, the closed topology of these 2D crystals, typically $R \approx 5$–$10\,\mu$m in radius, dictates at least twelve $+1$ disclinations, so that $\sum_\alpha q_\alpha = 6\chi$, where $\chi = 2$ is the Euler characteristic of the sphere [18]. The interplay between frustration, elasticity, and the unusual capillarity of interfacially frozen droplets gives rise to a rich landscape of nearly degenerate energy minima, which droplets can explore at the modest cost of a width of thermal fluctuations or buoyancy [16].

A thorough understanding of the emergent behavior of emulsion droplets is therefore inextricably connected with an accurate knowledge of the crystalline structure of the frozen oil-water interface and, particularly, the spatial organization of topological defects: disclinations, dislocations, and extended defect structures, like "scars"—i.e., chains of dipoles featuring a net topological charge [19]—and dislocation "clouds" [16]. Unlike in other spherical crystals where particles can be resolved via optical microscopy [20–23], the molecules comprising the frozen interface of emulsion droplets cannot be directly imaged. This limitation can be partially overcome by taking advantage of the spontaneous adsorption of fluorescent dye molecules onto *isolated* topological defects [24]. However, the possibility of using this method to resolve extended defect structures has never been explored, thereby preventing characterization of the defects' interfacial organization and hampering fundamental understanding and eventual technological application of these emulsions.

Here we employ fluorescent dye adsorption for the imaging of extended defect structures in interfacially frozen spherical crystals. This technique allows us to resolve the structure of spherical crystals with an unprecedentedly high number of lattice sites ($N \approx 10^9$), revealing an unanticipated uncoiling transition, where globular clusters of dislocations—referred to as clouds—uncoil into threadlike structures similar to complex scars. Our experimental results are rationalized using a theoretical model of extended defect structures [16,25] and

*Present address: Department of Bionanoscience, Kavli Institute of Nanoscience, Delft University of Technology, The Netherlands.
†Contact author: giomi@lorentz.leidenuniv.nl
‡Contact author: eli.sloutskin@biu.ac.il

Monte Carlo (MC) simulations, which make no assumptions of our theoretical model.

II. FLUORESCENT PATTERNS: EXPERIMENTAL OBSERVATIONS

To form oil-in-water emulsions exhibiting interfacial freezing, we suspend pure linear *n*-alkane $H(CH_2)_nH$ oil (denoted $C_n; n = 12 - 18$) droplets in an aqueous solution of sodium hexadecyl sulfate $CH_3(CH_2)_{15}OSO_3Na$ surfactant (denoted SHS) [24]. The fluorescent dye rhodamine B is added to the water phase to visualize the topological defects in the interfacially frozen monolayer (see Appendix A 1). To control the repulsions between the water-ionized surface-adsorbed SHS surfactant anions, we add CsCl to the water. The impact of various salts on surface freezing has been recently explored [26], and CsCl was chosen because, besides providing electrostatic screening, it stabilizes the SHS against precipitation.

For interfacial crystal defects' visualization, the fluorescent dye must exhibit high surface affinity [24]. When using rhodamine B, all droplets display brightly shining surfaces under fluorescent confocal microscopy at $T > T_s$, indicating extensive interfacial adsorption of the dye. This adsorption suggests that at $T > T_s$ the interfacial tension of a fluorescent dye-covered droplet (γ_f) is lower than that of a dye-free droplet γ_0: $\Delta\gamma = \gamma_f - \gamma_0 < 0$ (see Appendix A 2) [24]. Notably, while $\Delta\gamma$ is only weakly dependent on temperature at $T > T_s$, it develops a steep and negative slope at $T < T_s$ [see Fig. 1(a)]. This slope is dictated by the high and *positive* slope of γ_0 in the interfacially frozen regime [green line in Fig. 1(a)], demonstrated earlier to stem from the loss of (mainly, conformational) entropy by the interfacially frozen molecules [1–6,10,24,26,27]. Rhodamine B does not have an alkyl tail capable of the incorporation into the interfacially frozen monolayer, so that the dye-covered interface exhibits no interfacial freezing transitions and, consequently, γ_f is featureless [blue line in Fig. 1(a)] [27]. Therefore, the slope change in $\Delta\gamma$ is equal in magnitude to the one of γ_0. This situation contrasts with previous studies, where an alkyl tail-bearing $flC_{12}OH$ dye incorporated into the interfacially frozen monolayer, so that γ_f exhibited a significant slope change and the slope steepness of $\Delta\gamma$ at $T < T_s$ was consequently reduced. Notably, while the lower-slope $flC_{12}OH$ system is easier to temperature control, the presently used rhodamine-B system has the advantage of being simpler, as it does not form a mixed three-component dye:alkane:surfactant crystal. As a result of the slope change in $\Delta\gamma$, it vanishes at $T = T_x < T_s$ and switches positive on cooling to $T < T_x$, eventually driving the fluorescent dye off the droplets' interfaces [24]. Note that when the droplet's surface is covered by a crystalline monolayer, the interfacial dye adsorption depends not only on $\Delta\gamma$ but also on the elastic energy of the interfacial crystal. The elastic energy density, in turn, is nonuniform, but peaks at the defects' locations. Therefore, on cooling below T_x, the dye first desorbs from surface positions with a low elastic energy density, followed by a complete desorption at a lower T. Conversely, on reheating, the dye first readsorbs at the near-defect, high elastic energy density positions, forming well-defined fluorescent patterns, then fully covers the whole surface at T_x.

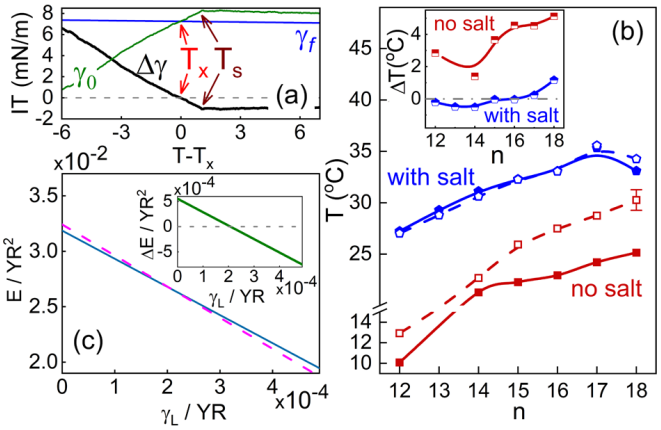

FIG. 1. (a) The interfacial tension (IT) of a dye-free interface, γ_0 (green line), exhibits a slope change at T_s. Since the IT of a dye-covered interface, γ_f (blue line), is nearly constant on this scale, the difference between these two ITs, $\Delta\gamma = \gamma_f - \gamma_0$ (thick black line) slopes steeply at $T < T_s$. (b) For salt-doped systems (in blue; 140 mM), the experimental temperatures of complete fluorescent dye desorption from droplets' surfaces in a cooling scan (full symbols) closely match the temperatures where the pattern first forms on heating (open symbols) for all alkane chain lengths n. A large hysteresis ΔT between these two temperatures is exhibited in salt-free emulsions (red; see also the inset). Curves are guides to the eye. (c) The total energy of a simulated pattern incorporating only the 12 compact patches at disclination positions (pink dashes) and of a scars' pattern (blue solid line) vary with the dye patches' LT, γ_L. While the scars' pattern is energetically favorable at low γ_L, patch compaction takes place at higher γ_L. The inset shows the difference ΔE between the two energies.

Remarkably, the fluorescent patterns on our droplets are neither disordered nor unique, but feature two fundamental structural motifs. Salt-free systems exhibit 12 rounded patches, the centers of which are maximally separated on the droplet's surface [Fig. 2(a)]. This motif reproduces for all alkanes in our chain length range ($n = 12 - 18$), but depends on the ionic strength of the suspending aqueous solution. Specifically, increasing the salt concentration to 70 mM causes a prominent elongation of the patches [Fig. 2(b) and Supplemental Material Video 1 [28]]. At an even higher salt concentration (140 mM CsCl), the patches transform into a pattern of 12 scarlike curves [Fig. 2(c)].

III. CONTINUUM ELASTICITY MODEL

A. Dislocation scars

The crossover between the rounded and the scarlike patches is strikingly similar to the break-up of isolated 5-fold disclinations (i.e., $q_\alpha = +1$) into $5 - 7 - 5$ scars [18]. This phenomenon, predicted in the context of the Thomson problem [19] and verified in colloid experiments [21], is observed in crystals whose density is sufficiently large to render the geometry effectively flat at the scale of a lattice spacing, i.e., the crossover takes place at $N \approx 360$ [19,21,25]. The latter, however, is in manifest contradiction with the experimental observation of compact

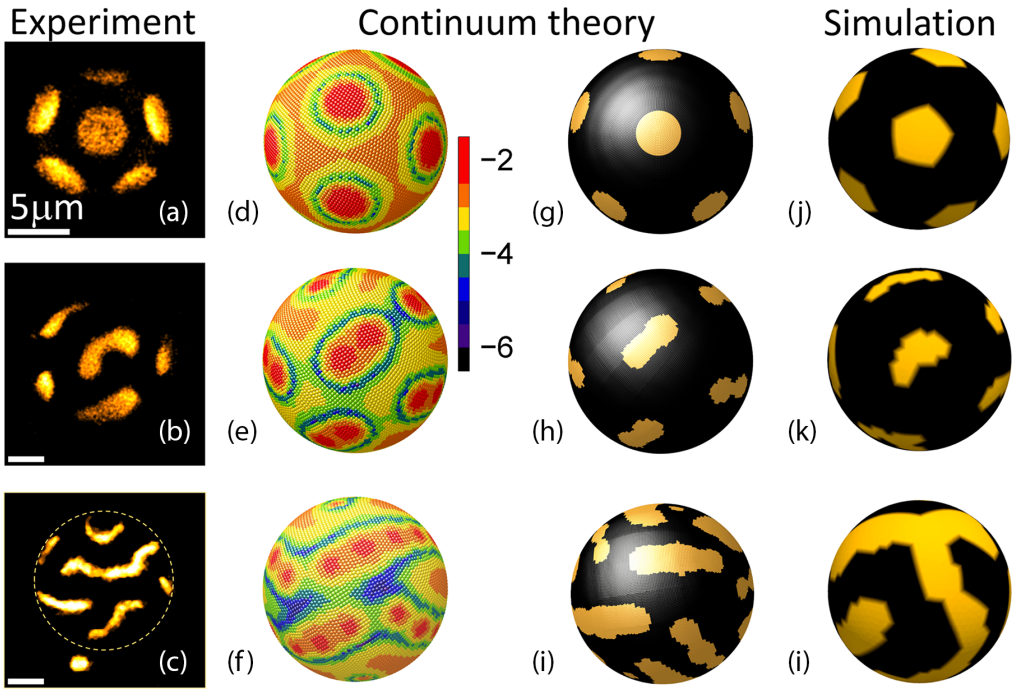

FIG. 2. (a) Twelve rounded fluorescent patches at the surface of a C_{12}-alkane experimental liquid droplet. (b) A pattern of 12 elongated fluorescent patches forms when salt is introduced into the aqueous medium (70 mM CsCl). (c) Long fluorescent scars are formed at a high salt concentration (140 mM CsCl). Dashes mark the droplet's edges. (d)–(f) Elastic energy density maps for $s = 0$, 0.38 and $0.75R$, corresponding to $\Gamma_L \gtrsim 8 \times 10^{-3} YR$, $\Gamma_L \approx 2.3 \times 10^{-3} YR$, and $\Gamma_L = 0$, respectively. The color scale bar values correspond to $\log_{10} \sigma^2$. (g)–(i) Dye adsorption patterns corresponding to maps in (d)–(f). The patterns are obtained for $\Delta\gamma = 1.2 \times 10^{-3}$, 1.4×10^{-3}, and $5.2 \times 10^{-4} Y$, respectively. (j)–(l) Discrete lattice simulations. $\gamma_L = 2.2 \times 10^{-4}$, 6.1×10^{-5}, and $4.1 \times 10^{-5} YR$, respectively. Note the excellent agreement with the experiment.

patches in Fig. 2(a), as the interfacial crystals comprise $N \approx 10^9$, far beyond the crossover value.

To resolve this apparent inconsistency, shedding light onto the patterns in Figs. 2(a)–2(c), we employ a continuum model of extended defect structures [16]. In this approach, dislocations are described by Burgers vectors, $\mathbf{b}$, characterizing the amount by which the translational long-range order is disrupted by each of the dislocations [29]. At the continuum level, the *density* of dislocations is expressed via a local Burgers vector density field [16]: $\mathbf{B} = \mathbf{B}(\mathbf{r}) = \sum_\beta \mathbf{b}_\beta \delta(\mathbf{r} - \mathbf{r}_\beta)$, where the summation is over all dislocations, located at positions $\{\mathbf{r}_\beta\}$. We also define a $\mathbf{B}$-perpendicular vector field $\mathbf{P} = \mathbf{P}(\mathbf{r})$, representing the dislocation polarization density. Its components are: $P^i = \epsilon^{ij} B_j$, where ϵ^{ij} is the Levi-Civita symbol [16]. This model assumes that, whether organized in clouds, scars, or otherwise, the distribution of $5-7$ dislocations proliferating in proximity of a *seed* (here, an isolated 5-fold disclination) can be described by the flux Φ of the dislocations emanating from the seed,

$$-\int_D dA \nabla_\perp \times \mathbf{B} = \oint_C ds \mathbf{n} \cdot \mathbf{P} = \Phi, \tag{1}$$

where $\nabla_\perp \times$ is the two-dimensional curl of a tangent vector and the integration is carried out over the area D or the boundary C of a small crystal patch, centered around the seed disclination and not containing any other disclination [16,25].

The crystal's stretching energy is

$$E_s = \frac{Y}{2} \int \mathrm{d}A \, \sigma^2 + E_c, \tag{2}$$

with Y the Young's modulus, $\sigma = \sigma(\boldsymbol{r})$ a dimensionless stress field [16], and E_c—the so-called core energy—providing the energy contribution at the defect core scale. In the absence of thermal fluctuations, the energy-minimizing σ configuration is

$$\nabla^2 \sigma = \frac{\pi}{3} \sum_{\alpha=1}^{N_{\text{seed}}} q_\alpha^{\text{eff}} \delta(\boldsymbol{r} - \boldsymbol{r}_\alpha) + \frac{\pi}{3} \sum_{\gamma=1}^{N_{\text{sink}}} q_\gamma^{\text{eff}} \delta(\boldsymbol{r} - \boldsymbol{r}_\gamma) - R^{-2}, \tag{3}$$

where ∇^2 is the Laplace-Beltrami operator on the sphere and the spherical vectors $\{\boldsymbol{r}_\alpha\}$ mark the positions of the N_{seed} seeding disclinations. $q_\alpha^{\text{eff}} = 1 - \Phi_\alpha/(\pi/3)$ is the effective topological charge of the αth defect complex, inclusive of the screening effect of the surrounding dislocations [25]. Due to the total topological charge conservation, the dislocation flux emanating from the seeding disclinations must be neutralized by an arbitrary number N_{sink} of *sinks*. Assuming $N_{\text{seed}} = 12$ and $\Phi_\alpha = \Phi$ for $\alpha = 1, 2 \ldots 12$ implies $q_\gamma^{\text{eff}} = (N_{\text{seed}}/N_{\text{sink}})[\Phi/(\pi/3)]$.

Following experimental evidence [21,22,30], we assume the 12 seeds to be positioned at the vertices of a sphere-inscribed regular icosahedron with two sinks at a geodesic distance $\pm s/2$ from each seed, so that the three points are aligned along the same great circle and collectively carry a unitary *effective* topological charge (see Fig. 3). The orientation of the great circle at each disclination is chosen to

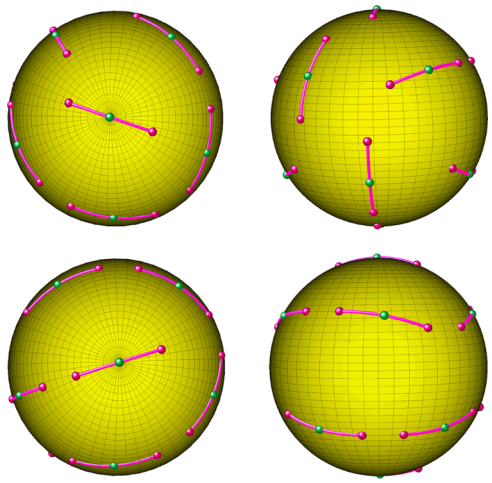

FIG. 3. The optimal orientations of the 12 dislocation scars of length $s = 0.75R$ (magenta). The 24 sink positions $\{\mathbf{r}_\gamma\}$ are shown in purple. The seed disclination positions $\{\mathbf{r}_\alpha\}$ are shown in green. The four panels correspond to different view directions.

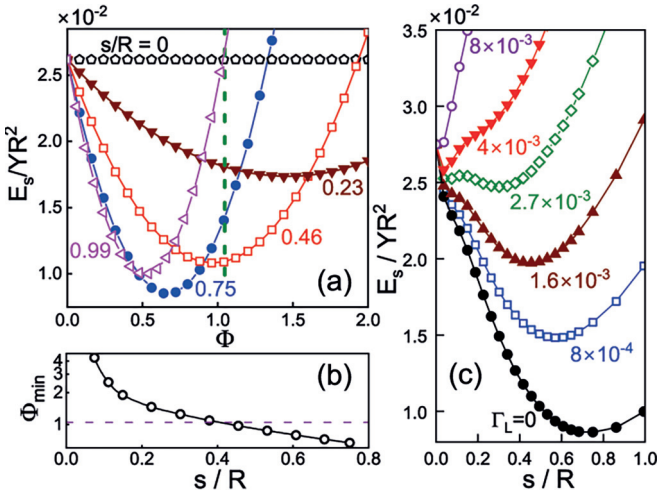

FIG. 4. (a) The extensional energy of a spherical crystal E_s, with the defect core energy neglected, for several different dimensionless scar lengths s/R (see labels), exhibits a minimum at $\Phi = \Phi_{\min}$. Notably, if $\Phi_{\min} > \pi/3$ (vertical green dashes), charge sign inversion takes place at the 12 disclination positions. (b) The E_s-minimizing Φ value increases for short scar lengths. The charge sign inversion conditions are marked by dashes. (c) When the core energy of the dislocation scars is taken into account, a finite scar's LT, Γ_L, emerges (see labels, in YR units). The corresponding Φ-optimized extensional energy $E_s(\Phi_{\min})$ exhibits a minimum at a Γ_L-dependent scar length, enabling scar length control by Γ_L.

maximize the distance between the sinks (see Appendix B 1). This construction, together with Eq. (3), is suited to mimic the configuration of the stress field σ at large distances from the seed for either the isotropic patches ($s \ll R$) or scarlike structures ($s \approx R$). Note that this construction is different from the icosahedrally symmetric one, which has been employed in previous theoretical studies, assuming five dislocation scars to emanate from each of the 12 seeding disclinations [16,19,25].

To obtain s and Φ, we minimize the E_s over these variables, assuming $E_c = 0$ (see Appendix B 2). The typical $E_s(\Phi)$, for several different s, are shown in Fig. 4(a). The absolute minimum is obtained for $s \approx 0.75R$ and $\Phi \approx 0.65$. Here, the topological defects form long scars, interwinding across the sphere [see the stress map in Fig. 2(f); cf. to Fig. 2(c)]. For $s < 0.4R$, however, the energy-minimizing Φ value exceeds $\pi/3$, so that the effective charge q_α^{eff} of the seeds crossovers from positive to negative [Fig. 4(b)]. This crossover corresponds to the aforementioned transition from isolated disclinations to scars. When $\Phi = 0$, the effective charge of each defect complex q_α^{eff} equates that of a $5-7-5$ scar. Since for such a scar $s = 2a$, where a is the lattice constant, the critical condition $s/R = 0.4$ (thus $a = R/5$) implies $N = 4\pi R^2/A_V \approx 363$ ($A_V = \sqrt{3}/2\, a^2$ is the area of the Voronoi cell enclosing each particle), in perfect agreement with previous observations [21] and predictions [19].

B. Core energies induce scar line tension

While convincingly confirming our theoretical model, the above is, however, insufficient to explain the observed uncoiling clouds-to-scars transition. A possible control knob for the scar length is provided by the core energy E_c: i.e., the energy at the microscopic core radius R_c, where the continuum description inevitably breaks down. In the case of isolated defects, $E_c = \sum_i q_i^2 \epsilon_i$—where $\epsilon_i \sim R_c^2$ is a constant proportional to the area of the ith defect core—and is negligible, as long as R_c is much smaller than the system size [31]. However, in the case of extended defect structures, E_c cannot be neglected. To capture the transition from clouds to scars, we approximate the core region as an ellipse of aspect ratio $r > 1$, so that $\sum_i q_i^2 \epsilon_i \approx 12\Gamma\pi r R_c^2$, where Γ is a constant with dimensions of surface tension. Assuming R_c to be fixed at the transition and taking $s = rR_c$, we obtain $E_c = 12\Gamma_L s$, where $\Gamma_L = \Gamma\pi R_c$ is an effective line tension (LT) of the defect complex. An order of magnitude Γ_L estimate [29] is provided by the energy of fusion $\Delta E_f \approx 20\, k_B T$ of a C_{16} alkane molecule, the midpoint of the alkane n-range studied here. As the lattice constant of our crystal is [4] $a \approx 5$ Å, we estimate $\Gamma_L \approx \Delta E_f/a$, yielding for a typical $R \approx 10\,\mu$m droplet a significant scar energy: $s\Gamma_L \approx R(\Delta E_f/a) \approx 4 \times 10^5\, k_B T$. Thus, with the previously established Y limits [1]: $6 \times 10^{-4} < Y < 0.04$ N/m, we obtain $4 \times 10^{-4} \lesssim \Gamma_L/YR \lesssim 3 \times 10^{-2}$. We introduce the corresponding energy term into E_s, minimize over Φ, and demonstrate that the E-minimizing s value strongly depends on Γ_L in the experimentally relevant range of Γ_L values [Fig. 4(c)]. For $\Gamma_L \gtrsim 8 \times 10^{-3} YR$, no scars are formed, with only the 12 clouds remaining at the droplets' surfaces. Note the excellent agreement of the resulting surface maps [Figs. 2(d)–2(f)] with the experimental patterns [Figs. 2(a)–2(c)], strongly supporting the possibility that the increased screening of the ionic SHS headgroups' electrostatic fields at high salt concentrations diminishes the value of Γ_L/YR. Since previous studies detected no significant salt-induced variation of γ at the droplets' self-faceting transition [26], Y must stay virtually unchanged over the relevant salt concentration range; an *increase* in Y at a high screening is particularly unlikely. Therefore, we attribute the Γ_L/YR variation to a reduction in Γ_L: the defects' core energy is reduced by the electrostatic fields' screening.

To reproduce the experimentally observed dye adsorption with our model, we note that the fluorescent patches are formed at $T < T_x$, where dye-covered regions have a higher interfacial tension, since $\Delta\gamma > 0$. Consequently, while dye adsorption onto a surface area dA alleviates the stress energy by $dE_s = (Y/2)\sigma^2 dA$, it also invokes a cost $\Delta\gamma dA$ due to the increase in interfacial tension. The balance between the position-dependent elastic energy density and $\Delta\gamma$ gives rise to the formation of patterns and their coalescence at $T = T_x$, where $\Delta\gamma = 0$. The corresponding fluorescent maps [Figs. 2(g)–2(i)] are obtained as $H[(Y/2)\sigma^2 - \Delta\gamma(T)]$, where H is the Heaviside step function, and the adsorbate density is taken, for simplicity, to be discrete: either 0 or 1. The similarity between these patterns and the experimentally observed ones [Figs. 2(a)–2(c)] is remarkable (see also the left panels in Supplemental Material Videos 2 and 3). Yet, there is also an important difference: the number of patches in Supplemental Material Video 3 (left panel) suddenly increases at $\Delta\gamma/Y = 8 \times 10^{-4}$, with several triangular patches formed. Such events were not hitherto observed experimentally [24].

C. Line tension of the fluorescent patches

A clue for the origin of the experiment-theory disagreement in the number of patches is provided by the experimental observation that the temperature where the fluorescent dye is completely driven off the droplets' interfaces exhibits a significant hysteresis for the salt-free emulsions [Fig. 1(b)]. Remarkably, the hysteresis is almost zero in salt-containing systems [Fig. 1(b)]. Since either dye adsorption or dye desorption increases the boundary length between the dye-covered and the dye-free regions, the hysteresis may be a result of a finite LT γ_L of these boundaries. The incorporation of γ_L into our model [24] (see Appendix B 3) allows the superfluous triangular patches to be eliminated (Supplemental Material Video 3; right panel), enabling a realistic reproduction of the experimental patterns (Supplemental Material Videos 2 and 3).

IV. COMPUTER SIMULATION MODEL

To further support the proposed mechanism, we reproduce the patterns by direct simulations. We model the interfacial crystal by a spherical triangulation mesh of Hookean springs [32], where each vertex is assigned a spin of 1/2, with $S = +1$ (up) and $S = -1$ (down) spins denoting dye-covered and dye-free sites, respectively. The elastic energy is modeled by

$$E_s = \frac{1}{2}\Sigma_{i>j} k(|\boldsymbol{r}_i - \boldsymbol{r}_j| - a)^2 \left\{\frac{2 - (S_i + S_j)}{4}\right\}, \qquad (4)$$

where the summed-over (i, j) nearest-neighbor vertex positions are $(\boldsymbol{r}_i, \boldsymbol{r}_j)$, k is the spring constant, and a the relaxed spring's length. The dye-covered vertices are free of elastic energy but incur an extra energy $\Delta\gamma A_s$, where $A_s = 4\pi R^2/N$ is the surface area represented by the lattice site. To account for γ_L, we introduce a ferromagnetic interaction $E_{LT} = (-J/2)\Sigma_{i,j} S_i S_j$, where $J = \gamma_L A_s^{1/2} \geqslant 0$ and the summation is over all pairs of nearest neighbors (see Appendix C). Importantly, earlier simulations employing a similar Hamiltonian did not allow for the formation of dislocations [24], which are the focus of our present paper. In our present simulations, we enable dislocations' formation and annihilation through flipping of bonds between the adjacent vertices. The total energy is minimized by Monte Carlo annealing, where we first set all spins down, allow for vertices' displacements, and optimize the connectivity by bond flipping [32]. Then we repeat the annealing, allowing the spins to flip, with all other degrees of freedom kept fixed. This procedure allows γ_L-controlled switching between the short and the long scars' patterns [Figs. 2(k)–2(l)]. Importantly, the dislocation core energy is implicit in this model's discretization of the interfacial crystal's lattice, so that Γ_L cannot be varied independently. Since the formation of compact patches, where $s \to 0$, requires high γ_L, challenging the search of the global energy minimum, we avoid the bond flipping procedure in this case [Fig. 2(j)]. To confirm that the pattern consisting of compact patches is energetically favorable at high γ_L, we directly compare its total energy with the energy of a pattern of elongated scars, demonstrating that patch compaction lowers the energy for $\gamma_L > 2.1 \times 10^{-4} YR$ [Fig. 1(c)], in strong support of the proposed pattern control mechanism. Interestingly, while branched patterns, as in the simulated Fig. 2(l), were not allowed in our continuum model, such patterns have been previously reported in experiments employing the $\mathrm{flC_{12}OH}$ dye [24], suggesting an even lower γ_L than achievable with rhodamine B.

V. CONCLUSIONS

We have demonstrated that the fluorescent adsorption patterns on interfacially frozen liquid droplets can be controllably tuned by salt concentration adjustment, revealing unique defect complexes and transitions among them, in crystals of unprecedented size. Our combined experimental and theoretical analysis demonstrates that an effective LT, due to the defects' core energy, tunes the geometry of the extended defect structures. When LT is negligibly small, the formation of extended scars and elongated fluorescent patches is energetically favorable. When the LT is high, the elastic energy map is dominated by 12 dislocation clouds and the fluorescent patches are rounded. Thus, even though the geometry is effectively flat at the scale of the lattice spacing, the scars coil into clouds, to reduce their core energy. Plausibly, the decrease of LT at an elevated ionic strength is resulted by the enhanced electrostatic screening of Coulomb repulsions between the ionic surfactants' headgroups. Future experimental and theoretical studies, focusing onto the specifics of molecular scale interactions, may allow the precise mechanism of LT control to be established, paving, together with our present paper, unique pathways in self-assembly and elucidating the fundamental elasticity of 2D crystals frustrated by the spherical surface geometry.

ACKNOWLEDGMENTS

We thank S. Das and Y. Mastai for rhodamine B purification and acknowledge M. Deutsch for insightful discussions.

This research is supported by the Israel Science Foundation [Grant No. 2205/21 (E.S.)]. We thank the Kahn Foundation for the funding of the equipment. D.M.F. thanks the Comunidad de Madrid and the Complutense University of Madrid (Spain) through the Atraccion de Talento Program No. 2022-T1/TIC-24007.

APPENDIX A: EXPERIMENTAL METHODS

1. Emulsion preparation and optical microscopy measurement

First, a 0.4 mM aqueous stock solution of the SHS surfactant was prepared. Next, the fluorescent rhodamine B dye was added to this solution at a mass fraction $\approx 8 \times 10^{-8}$. For the formation of salt-containing emulsions, 70 or 140 mM of CsCl was introduced into the same solution. Note that in the presently studied range of salt concentrations, the effect of salt on the interfacial freezing temperature T_s is almost negligible [26], easing the comparison between salt-containing and salt-free samples. In all cases, the solution was stirred by a magnetic stirrer at $T \approx 50\,^{\circ}$C to ensure complete homogenization. Emulsions were prepared by admixing 1–2 mass-% alkane into the stock solution heated to $>50\,^{\circ}$C. The emulsions were stirred by a magnetic stirrer for $1-2$ min at $T \gtrsim 50\,^{\circ}$C. The emulsion is then kept at $T > 50^{\circ}$C, well above any possible droplet shape transitions [1,3].

For light microscopy measurements, we load the emulsion by capillary forces into Vitrocom $0.1 \times 2 \times 50$ mm rectangular glass capillary. During the loading of the capillaries, both the bulk material and the capillary are held at $T \geqslant 50\,^{\circ}$C. The capillary is then sealed and glued by instant epoxy glue, wide-face-down onto a brass platelet, having a narrow opening for optical observations and attached to a temperature-controlled baseplate. The baseplate resides on the MS-2000 ASI high-accuracy translation stage, mounted on an inverted Nikon Ti-E-based A1R laser scanning confocal microscope. The baseplate's temperature is controlled to $<0.01\,^{\circ}$C by a Lake Shore 330 PID controller employing a $100k\Omega$ precision thermistor and Peltier elements. The typical temperature scan rate was $6 \times 10^{-3}\,^{\circ}$C/s.

For microscopy, we employ a dry Plan Apo 20x (NA = 0.75) objective. A Nikon DS-Fi1 CCD camera was employed for bright field microscopy video acquisition. For confocal measurements, the fluorescent dye was excited by a 514 nm solid state laser, and frames of 512×512 pixels recorded, with the galvanometric mode employed for laser scanning. Note that bright field microscopy and confocal imaging serve in our studies as complementary techniques. In particular, the rhodamine B dye is fluorescent, so it is clearly visible by confocal microscopy but cannot be resolved by the bright field microscopy. Conversely, the alkane bulk of the droplets is nonfluorescent, so the shape of the droplet is clearly visible by the bright field microscopy yet *invisible* by the confocal microscopy. Our setup enables switching between the two complementary visualization modes in real time.

2. $\Delta\gamma$ measurements

To obtain the $\Delta\gamma$ data shown in Fig. 1(a), we first measured the liquid-liquid interfacial tension $\gamma_0(T)$ between bulk C_{16} alkane and bulk, dye-free, 0.4 mM aqueous SHS solution. These measurements were carried out by the Wilhelmy plate method [1,24,33], employing a 41-mm circumference glass plate. The sample, contained in a glass beaker, was held inside a two-stage oven, with an inner temperature-controlled ($\pm 0.01\,^{\circ}$C) cell residing inside a passive outer aluminum cell. All glassware contacting the sample were cleaned with a fresh hot Piranha solution, then thoroughly rinsed with Millipore water to avoid impurities. The measurement starts by a full immersion of the Wilhelmy plate in the aqueous phase. Next, the oil phase is added on top of the aqueous phase and the Wilhelmy plate is lifted to have its bottom edge touch the oil-water interface. The pull applied by the interface onto the Wilhelmy plate is measured by an electronic Precisa semimicro balance. Temperature scanning, recording the balance readings, and their conversion to interfacial tension are computerized. The scan employs $0.1 - 0.14\,^{\circ}$C steps, waiting 30 s after each step. Twenty measurements are averaged at each temperature, improving the smoothness of the $\gamma_0(T)$ curve.

Next, we measure the interfacial tension γ_{RB} of a similar liquid-liquid system, with the rhodamine-B fluorescent dye contained in the aqueous phase (mass fraction $\approx 8 \times 10^{-8}$). The same method is employed as above. Since rhodamine-B molecules do not have alkyl tails and therefore cannot be incorporated into the interfacial crystal, these molecules completely desorb from the planar interface at $T = T_x$, where the interfacial freezing of the *dye-containing* sample takes place. Therefore, at $T < T_x$, the Wilhelmy plate measurements of a dye-containing sample probe a dye-free interface, so that $\gamma_{RB}(T < T_x) = \gamma_0(T < T_x)$. As the spontaneous desorption of the dye does not allow the true interfacial tension γ_f of a dye-*covered* interface to be directly measured at $T < T_x$, we estimate γ_f in this temperature range by the extrapolation of γ_{RB} from $T > T_x$ to $T < T_x$. As for most typical disordered liquid interfaces, γ_{RB} is almost perfectly linear at $T > T_x$: $\gamma_{RB} = 13.6 - 0.021T$ mN/m. Thus, we obtain $\Delta\gamma(T) \approx 13.6 - 0.021T - \gamma_0(T)$. Note that a more complex behavior of γ_f occurred for the previously studied alcohol derivative of rhodamine B ($flC_{12}OH$), which possessed an alkyl tail potentially allowing the incorporation of dye molecules into the interfacial crystal [24]. The corresponding $\Delta\gamma$ had a lower temperature slope at $T < T_x$, facilitating the temperature control of the fluorescent pattern's coarsening, as described elsewhere [24].

Notably, since the concentration of the fluorescent dye is very low, its adsorption (or nonadsorption) to a defect-free interface is simply determined by the sign of $\Delta\gamma$, as described in the main text. This fact is demonstrated, e.g., by the classical Gibbs adsorption relation,

$$\Gamma = -\frac{1}{RT}\frac{\partial\gamma}{\partial lna}, \tag{A1}$$

where Γ is the adsorption, a is the activity of the dye, and R is the universal gas constant. When the concentration of the dye is low, as in our present study, a is equal to the dye's volume fraction. Consequently, for the adsorption to take place (i.e., $\Gamma > 0$), γ should decrease with the concentration of the dye. This is indeed the case at $T > T_x$, but not at $T < T_x$, so, in the absence of elastic contributions, the dye desorbs from the interface upon cooling to $T < T_x$.

APPENDIX B: CONTINUUM ELASTICITY MODEL

1. Scar positions and orientations

To obtain the dimensionless stress field $\sigma(\mathbf{r})$, we first choose the positions of the 12 seed disclinations $\{\mathbf{r}_\alpha\}$ and of the $12 \times 2 = 24$ sinks $\{\mathbf{r}_\gamma\}$. In particular, we assume that the 12 seed disclinations, subject to elasticity-mediated repulsions, are maximally separated on the surface of the sphere, so that $\{\mathbf{r}_\alpha\}$ points are at the vertex positions of a sphere-inscribed icosahedron [18–20,30,34]. This assumption is strongly supported by experiments [1,20,21,24] and theoretical calculations [18,19,30,34]. The dislocation scars are assumed to have their centers located at the $\{\mathbf{r}_\alpha\}$ positions and to follow the spheres' geodesics. Since the topological charges at the sinks repel each other, the scars' orientations should maximize the distance between the sinks, as also the sinks' distances from the (other scars') seed disclinations. In view of the repulsions between the sinks and the disclinations, one end of each scar is assumed to point along the geodesic which connects the disclination at the scar's center to one of its five *next*-nearest neighbor disclinations. This orientation maximizes the distance between the corresponding scar's endpoint and the *nearest*-neighbor disclinations, but also implies that the second end of the scar propagates towards one of the nearest-neighbor disclinations. This choice of scar orientations is motivated by symmetry considerations, as also by several earlier experimental [21,30] and theoretical [19] studies of spherical crystals. Note that the adopted symmetry still allows five different orientations for each of the twelve scars. Out of these possible orientations, we choose the one which maximizes the sum of sink-to-sink geodesic distances with the scar length chosen as $s = 0.75R$. The resulting scar orientations are demonstrated in Fig. 3.

2. Evaluation of the extensional stress energy

To solve the Poisson equation [Eq. (3)] for $\sigma(\theta, \phi)$, where θ and ϕ are the polar and the azimuthal angles, we first rewrite this equation as

$$\nabla^2\sigma = \frac{\pi}{3}\sum_j q_j^{\text{eff}}\delta(\mathbf{r} - \mathbf{r}_j) - R^{-2}, \tag{B1}$$

where R is the radius of the spherical surface, and j sums over the $N_{\text{disc}} = 12$ disclinations of effective topological charge q_α^{eff}, residing at positions $\{\mathbf{r}_\alpha\}$ and over the $N_{\text{sink}} = 24$ sinks of charge q_γ^{eff}, residing at $\{\mathbf{r}_\gamma\}$. As discussed in the main text,

$$q_\alpha^{\text{eff}} = 1 - \Phi/(\pi/3) \tag{B2}$$

and

$$q_\gamma^{\text{eff}} = (N_{\text{disc}}/N_{\text{sink}})[\Phi/(\pi/3)], \tag{B3}$$

where Φ is the unknown flux of dislocations emanating from the seed. As in a previous study [25], we solve Eq. (B1) by Sturm-Liouville decomposition of $\sigma(\theta, \phi)$, employing the spherical harmonics,

$$Y_l^m(\theta, \phi) = \sqrt{(2l + 1\frac{(l-m)!}{(l+m)!}}P_l^m(cos(\theta))e^{im\phi}, \tag{B4}$$

as the eigenfunctions. Here P_l^m are the associated Legendre functions including the Condon-Shortley phase $(-1)^m$ and the normalization is

$$\frac{1}{A}\int dA Y_l^m Y_l^{m^*} = \delta_{nm}. \tag{B5}$$

The stretching energy E_s is obtained as [25,35]

$$\frac{E_s}{YR^2} = \frac{\pi}{72}\sum_{l\geqslant 1}^{L_{\max}}\sum_{m\geqslant -l}^{l}\frac{1}{l^2(l+1)^2}\left|\sum_j q_j^{\text{eff}}Y_l^m(\theta_j, \phi_j)\right|^2, \tag{B6}$$

where Y is the 2D Young's modulus, (θ_j, ϕ_j) are the coordinates of disclinations and sinks, and $L_{\max}$ is the cutoff term above which this expansion is truncated for numerical evaluation. We use $L_{\max} = 50$, since the corrections due to higher harmonics are negligibly small. Finally, the $\sigma(\theta, \phi)$ map is obtained as

$$\sigma(\theta, \phi) = \sum_{l\geqslant 1}^{L_{\max}}\sum_{m\geqslant -l}^{l}\left[\frac{1}{12l(l+1)}\sum_j q_j^{\text{eff}}Y_l^m(\theta_j, \phi_j)\right]Y_l^m(\theta, \phi), \tag{B7}$$

yielding the stretching energy density (for zero core energy, E_c):

$$\epsilon(\theta, \phi) = \frac{Y}{2}\sigma^2(\theta, \phi). \tag{B8}$$

For a given s, we first calculate $E_s(\Phi)$ [Eq. (B6)] and find the value of Φ which minimizes $E_s(\Phi)$. The E_s-minimizing value of Φ is then used to calculate the stress energy density maps, employing Eqs. (B7) and (B8) [Figs. 2(d)–2(f)]. As explained in the main text, to introduce the dislocation scar line tension, we add to E_s an extra term, $E_c = 12s\Gamma_L$. This additional term shifts the E_s-minimizing value of s [see Fig. 4(c)], but it has no influence on the $\epsilon(\theta, \phi)$ map obtained for a given s value.

3. Dye adsorption: energy minimization with a non-zero γ_L

To calculate the patterns of dye adsorption within the present elasticity model, we first discretize the $\epsilon(\theta, \phi)$ map. For that, we choose $N = 9998$ uniformly distributed sites on the spherical surface and distribute the elastic energy among these sites, by proximity. Thus, the extensional energy of the kth site is $\int_{A_s}\epsilon dA$, where $A_s = 4\pi R^2/N$ is the surface area represented by such a site. Each of the sites is assigned a spin-1/2. Down ($S = -1$) and up ($S = +1$) states of the spin denote dye-free and dye-covered sites, respectively. A dye-covered site is assumed to have a zero extensional energy, but such a site has an additional energy contribution $\Delta\gamma A_s$, reflecting the energy of adsorption. Note that $\Delta\gamma$ switches from positive to negative on heating above T_x [see Fig. 1(a)]. The line tension γ_L of a fluorescent patch is introduced by means of a ferromagnetic interaction term: $E_{\text{LT}} = (-J/2)\sum_{\langle ij\rangle} S_i S_j$, where $J = \gamma_L A_s^{1/2} \geqslant 0$ and the summation is over all pairs of nearest-neighbor sites, defined by proximity. To minimize the energy of our model, we carry out an annealing procedure, during which the spins are flipped according to the classical MC dynamics. For a given $\Delta\gamma$ and γ_L, the annealing was separately performed for 15 different s values, spanning the range $0 < s < 0.75$. The s value corresponding to the lowest total

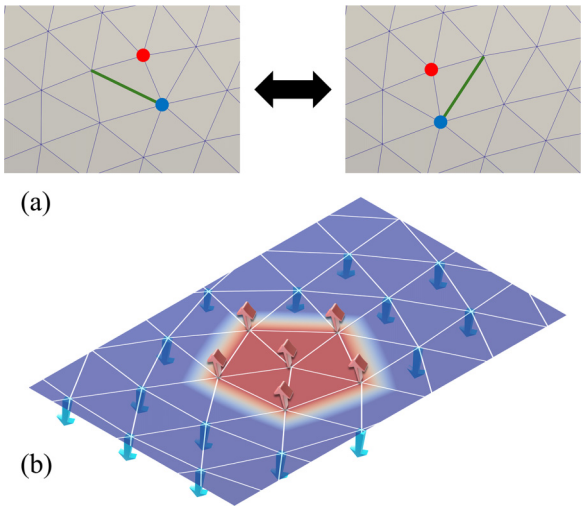

FIG. 5. (a) Edge flip: The edge marked in bold green in the left panel is replaced by the edge marked in green in the right panel and vice versa. The red and the blue dots denote a 5-fold (charge $= +1$) and a 7-fold (charge $= -1$) disclination, respectively. Note these defects' displacement upon the edge flip. (b) The spin-decorated lattice: The up and the down spins correspond to dye-covered and dye-free regions, respectively.

energy was then adopted. Note that this search for energy-minimizing s value was only necessary for the right panel of Supplemental Material Video 2, as the data in Supplemental Material Video 3 correspond to $\Gamma_L > 10^{-2}YR$, so that $s = 0$. The left panel of Supplemental Material Video 2 corresponds to $\gamma_L = 0$, so the patterns were obtained by a direct calculation (see main text) and no MC simulations of adsorption were necessary.

APPENDIX C: HOOKEAN SPRING LATTICE SIMULATIONS

To reproduce the fluorescent pattern by direct simulations, we employ the PyMembrane framework [32]. The interface is modeled by a lattice of $N = 2562$ vertices on a sphere of radius $R = 1$. Initially, the vertices are in the icosadeltahedral configuration, so the twelve 5-fold disclination defects are located at the tips' positions of an inscribed icosahedron. Each pair of nearest neighbors, defined by triangulation, are connected by a Hookean spring, so that the total stretching energy of the initial (dye-free) lattice is $E_s = (k/2)\Sigma_{i>j}(|r_i - r_j| - \tilde{a})^2$, where $k = \sqrt{3}Y/2$, $\tilde{a} = (4\pi/N)^{1/2} \approx 0.07R$ is the length of an unstrained edge, and the summation is carried out over all nearest-neighbor vertices [1]. For stability purposes, we also add a hard constraint, limiting the edge length to $0.7r_{\min} < |r_i - r_j| < 1.8r_{\max}$, where $r_{\min}$ and $r_{\max}$ are the shortest and the longest edges of the initial lattice configuration [32].

We relax the energy of our spherical lattice by MC dynamics, involving vertex displacements by $\Delta r \approx 10^{-3}R$ along the spherical surface and bond flips, where an edge (i.e., a spring) shared by two triangles of the lattice is removed and the two vertices opposite to it are reattached by a new edge (i.e., a new spring), as demonstrated in Fig. 5(a) [32]. The number of bond flip attempts was equal to the number of attempted vertex displacements. We start the relaxation with $T \approx 10^{-3}$ and $10^{-4}YR^2/k_B$ for edge flips and vertex displacements, respectively. At these T values, the corresponding degrees of freedom are unfrozen, allowing efficient probing of the phase space. Next, both temperatures were reduced in eight steps to $T \approx 10^{-6}$ and $10^{-5}YR^2/k_B$, respectively, with $10^4 - 10^6$ MC cycles done at each temperature. The energy was plotted as a function of the MC cycle number, at several T values, to confirm that the number of cycles and the choice of T values were adequate.

The described procedure produces an hexagonal lattice on a sphere, decorated by dislocation scars. Most of these scars are unbranched and their centers are roughly at the tips' positions of a sphere-inscribed icosahedron, supporting the assumptions of our continuum elasticity model. At this point, we disable the edge flips and the vertex displacements and assign each vertex a spin of 1/2, denoting dye-covered and dye-free sites [Fig. 5(b)], as described in the main text. The total energy includes three terms: $E_T = E_s + \Delta\gamma A_s \Sigma_i (S_i + 1)/2 + E_{LT}$, where $S_i = \pm 1$ is the spin state, the summation is carried out over all vertices, and the expressions for E_s and $E_{\rm LT}$ are given in the main text. To find the configuration of spins which minimizes E_T, we carry out MC annealing, with (only) the spin flip attempts allowed. The initial temperature is chosen as $T = 10^{-5}YR^2/k_B$. The final temperature is $T = 10^{-10}YR^2/k_B$. The annealing is done in six steps, in each of which T is reduced by a factor of 10, followed by 10^3 MC relaxation cycles. The resulting spin maps are shown in Figs. 2(k)–2(l), where up spins and down spins are orange and black, respectively. Figure 2(j) is obtained by a similar procedure, but with no edge flips allowed during the relaxation of the spherical lattice, so that no dislocation scars are formed.

[1] S. Guttman, Z. Sapir, M. Schultz, A. V. Butenko, B. M. Ocko, M. Deutsch, and E. Sloutskin, How faceted liquid droplets grow tails, Proc. Natl. Acad. Sci. USA **113**, 493 (2016).

[2] S. R. Liber, O. Marin, A. V. Butenko, R. Ron, L. Shool, A. Salomon, M. Deutsch, and E. Sloutskin, Polyhedral water droplets: Shape transitions and mechanism, J. Am. Chem. Soc. **142**, 8672 (2020).

[3] S. Guttman, E. Kesselman, A. Jacob, O. Marin, D. Danino, M. Deutsch, and E. Sloutskin, Nanostructures, faceting, and splitting in nanoliter to yoctoliter liquid droplets, Nano Lett. **19**, 3161 (2019).

[4] L. Tamam, D. Pontoni, Z. Sapir, S. Yefet, E. Sloutskin, B. M. Ocko, H. Reichert, and M. Deutsch, Modification of deeply buried hydrophobic interfaces by ionic surfactants, Proc. Natl. Acad. Sci. USA **108**, 5522 (2011).

[5] O. Marin, M. Tkachev, E. Sloutskin, and M. Deutsch, Polyhedral liquid droplets: Recent advances in elucidation and application, Curr. Opin. Colloid Interface Sci. **49**, 107 (2020).

[6] S. Hacmon, S. R. Liber, L. Shool, A. V. Butenko, A. Atkins, and E. Sloutskin, "Magic numbers" in self-faceting of alcohol-doped emulsion droplets, Small **19**, 2301637 (2023).

[7] S. Tcholakova, Z. Valkova, D. Cholakova, Z. Vinarov, I. Lesov, N. Denkov, and S. K. Smoukov, Efficient self-emulsification via cooling-heating cycles, Nat. Commun. **8**, 15012 (2017).

[8] D. Cholakova, M. Lisicki, S. K. Smoukov, S. Tcholakova, E. E. Lin, J. Chen, G. De Canio, E. Lauga, and N. Denkov, Spontaneous particle desorption and "Gorgon" drop formation from particle-armored oil drops upon cooling, Nat. Phys. **17**, 1050 (2021).

[9] D. Cholakova, N. Denkov, S. Tcholakova, I. Lesov, and S. K. Smoukov, Control of drop shape transformations in cooled emulsions, Adv. Colloid Interface Sci. **235**, 90 (2016).

[10] S. R. Liber, A. V. Butenko, M. Caspi, S. Guttman, M. Schultz, A. B. Schofield, M. Deutsch, and E. Sloutskin, Precise self-positioning of colloidal particles on liquid emulsion droplets, Langmuir **35**, 13053 (2019).

[11] D. Cholakova, Z. Valkova, S. Tcholakova, N. Denkov, and B. P. Binks, Spontaneous particle desorption and "Gorgon" drop formation from particle-armored oil drops upon cooling, Soft Matter **16**, 2480 (2020).

[12] E. Hsu, D. Lee, and E. Sloutskin, Non-classical Euler buckling and Brazier instability in cylindrical liquid droplets, Nano Lett. **24**, 8717 (2024).

[13] L. A. Hoffmann, L. N. Carenza, J. Eckert, and L. Giomi, Theory of defect-mediated morphogenesis, Sci. Adv. **8**, eabk2712 (2022).

[14] R. Gordon, M. M. Hanczyc, N. D. Denkov, M. A. Tiffany, and S. K. Smoukov, *Habitability of the Universe Before Earth*, Emergence of polygonal shapes in oil droplets and living cells: The potential role of tensegrity in the origin of life (Academic Press, USA, 2018), pp. 427–490.

[15] P. A. Haas, D. Cholakova, N. Denkov, R. E. Goldstein, and S. K. Smoukov, Shape-shifting polyhedral droplets, Phys. Rev. Res. **1**, 023017 (2019).

[16] I. García-Aguilar, P. Fonda, E. Sloutskin, and L. Giomi, Faceting and flattening of emulsion droplets: A mechanical model, Phys. Rev. Lett. **126**, 038001 (2021).

[17] H. Wan, G. Jeon, W. Xin, G. M. Grason, and M. M. Santore, Flower-shaped 2D crystals grown in curved fluid vesicle membranes, Nat. Commun. **15**, 3442 (2024).

[18] M. J. Bowick and L. Giomi, Two-dimensional matter: Order, curvature and defects, Adv. Phys. **58**, 449 (2009).

[19] M. J. Bowick, D. R. Nelson, and A. Travesset, Interacting topological defects on frozen topographies, Phys. Rev. B **62**, 8738 (2000).

[20] R. Guerra, C. P. Kelleher, A. D. Hollingsworth, and P. M. Chaikin, Freezing on a sphere, Nature (London) **554**, 346 (2018).

[21] A. Bausch, M. Bowick, A. Cacciuto, A. Dinsmore, M. Hsu, D. Nelson, M. Nikolaides, A. Travesset, and D. Weitz, Grain boundary scars and spherical crystallography, Science **299**, 1716 (2003).

[22] T. Einert, P. Lipowsky, J. Schilling, M. J. Bowick, and A. R. Bausch, Grain boundary scars on spherical crystals, Langmuir **21**, 12076 (2005).

[23] G. Meng, J. Paulose, D. R. Nelson, and V. N. Manoharan, Elastic instability of a crystal growing on a curved surface, Science **343**, 634 (2014).

[24] S. Das, A. V. Butenko, Y. Mastai, M. Deutsch, and E. Sloutskin, Topology-driven surface patterning of liquid spheres, Nat. Phys. **18**, 1177 (2022).

[25] I. García-Aguilar, P. Fonda, and L. Giomi, Dislocation screening in crystals with spherical topology, Phys. Rev. E **101**, 063005 (2020).

[26] P. M. Nanikashvili, A. V. Butenko, M. Deutsch, D. Lee, and E. Sloutskin, Salt-induced stability and modified interfacial energetics in self-faceting emulsion droplets, J. Colloid Interface Sci. **621**, 131 (2022).

[27] X. Z. Wu, B. M. Ocko, E. B. Sirota, S. K. Sinha, M. Deutsch, G. H. Cao, and M. W. Kim, Surface tension measurements of surface freezing in liquid normal alkanes, Science **261**, 1018 (1993).

[28] See Supplemental Material at http://link.aps.org/supplemental/10.1103/PhysRevResearch.6.043098 for experimental and theoretical videos.

[29] P. M. Chaikin and T. C. Lubensky, *Principles of Condensed Matter Physics* (Cambridge University Press, Cambridge, 1995).

[30] F. L. Jiménez, N. Stoop, R. Lagrange, J. Dunkel, and P. M. Reis, Curvature-controlled defect localization in elastic surface crystals, Phys. Rev. Lett. **116**, 104301 (2016).

[31] M. Kleman and O. D. Lavrentovich, *Soft Matter Physics: An Introduction* (Springer-Verlag, New York, 2003).

[32] D. A. Matoz-Fernandez, S. Li, M. O. de la Cruz, and R. Sknepnek, PyMembrane: A flexible framework for efficient simulations of elastic and liquid membranes, arXiv:2308.12754.

[33] S. Guttman, Z. Sapir, B. M. Ocko, M. Deutsch, and E. Sloutskin, Temperature-tuned faceting and shape-changes in liquid alkane droplets, Langmuir **33**, 1305 (2017).

[34] J. Lidmar, L. Mirny, and D. R. Nelson, Virus shapes and buckling transitions in spherical shells, Phys. Rev. E **68**, 051910 (2003).

[35] Note that a factor of 2 is missing for E_{stretch} in Fig. 3 of Ref. [25].